Nondegenerate chiral phonons in the Brillouin-zone center of $\sqrt{3} \times \sqrt{3}$ honeycomb superlattices

Xifang Xu, Hao Chen, and Lifa Zhang*
Center for Quantum Transport and Thermal Energy Science, School of Physics and Technology, Nanjing Normal University, Nanjing, 210023, China

(Received 13 May 2018; revised manuscript received 23 July 2018; published 8 October 2018)

The theoretical finding on chiral phonons at Brillouin-zone corners (valleys) of two-dimensional honeycomb lattices and its experimental verification in monolayer tungsten diselenide [H. Zhu, J. Yi, M. Li, J. Xiao, L. Zhang, C. Yang, R. A. Kaindl, L. Li, Y. Wang, and X. Zhang, Science **359**, 579 (2018)], have attracted wide attention in the study of phonon chirality very recently. In this paper, to make chiral phonons more measurable, the valley phonons were folded to Brillouin-zone center in $\sqrt{3} \times \sqrt{3}$ honeycomb superlattices, and near the center topological chiral phonons can be observed. The chiral phonons which are not the superposition of linear modes are nondegenerate and can be optically excited in helicity-resolved Raman scattering. Moreover, by adjusting the doping mass, the topological chiral phonons can be engineered in specific branches. Finally, in deformed $\sqrt{3} \times \sqrt{3}$ honeycomb superlattices, topological chiral phonons can also be found near the Brillouin-zone center. We believe that the findings of nondegenerate topological chiral phonons in the Brillouin-zone center help to enrich our understanding of chiral phonons and promote future applications in phononics.

DOI: 10.1103/PhysRevB.98.134304

I. INTRODUCTION

The Einstein-de Haas effect [1,2] has provided an effective method for measuring the gyromagnetic ratio in various materials [3–5] where the phonon angular momentum was taken to be zero. However, nonzero phonon angular momentum has been theoretically predicted in magnetic crystals with spin-phonon coupling [6], and the gyromagnetic ratio obtained through the Einstein-de Haas effect needs to be corrected by including the phonon contribution in the total angular momentum. In nonmagnetic materials without spin-phonon interactions where the time-reversal symmetry is conserved, the total phonon angular momentum is zero since the phonon angular momentum is an odd function of the wave vector. However, each phonon mode can have a nonzero phonon angular momentum in the honeycomb AB lattice with broken inversion symmetry, which means it can be elliptically or circularly polarized; that is, the phonon is chiral [7]. Particularly in Brillouin-zone corners—valleys $\boldsymbol{K}(\boldsymbol{K}')$, the phonon can either be right- or left-circularly polarized. Endowed with a quantized pseudoangular momentum, chiral phonons at valleys decide selection rules for intervalley scattering of electrons by phonons in valleytronics, an emerging field of manipulation of the valley degree of electrons [8–17]. The chiral phonons at valleys also have nonzero distinct phonon Berry curvature; then, under a strain gradient field a transverse phonon transport can emerge from valleys; that is, a valley phonon Hall effect can be observed [7]. Since the chiral phonon was predicted in a honeycomb AB lattice, the chiral phonons have also been found in Weyl semimetals [18], Kekulé lattice [19], bilayer triangle lattice [20], graphene boron nitride heterostructure [21], etc.

Very recently, chiral phonons were experimentally verified in monolayer WSe_2 [22], which is remarkable progress since it confirms that phonons, a kind of Bosonic quasiparticle, can attain chirality. Considering that the chiral phonons can be vastly excited by the optical pump-probe technique [22], it is possible to manipulate phonon chirality [23] and then pave the way in future phononic applications. The chiral phonons also play an important role in other fields [24,25], such as the control of topological states [26], the electronic phase transition [27,28], the intervalley scattering [13,14,29–33], as well as solid-state quantum information applications [34,35]. The finding of chiral phonons also promotes the progress of other fields such as the valley transport of sonic crystals [33], the polarization in two-dimensional (2D) materials [36], and so on.

As we know, the theoretical prediction and experimental verification of chiral phonons are concentrated on the valleys $\boldsymbol{K}(\boldsymbol{K}')$. The detection of valley phonons depends on the second-order interaction where the photon absorbtion and phonon emission coincide in the hole intervalley scattering, which is relatively complicated and difficult to measure. The work of helicity-resolved Raman scattering showed that the degenerate phonons at the Brillouin-zone center $\boldsymbol{\Gamma}$ can reverse the helicity of incident photons completely, where the involved $\boldsymbol{\Gamma}$ phonons attain chirality by superposition of the degenerated modes [37]. Actually, the two inequivalent valleys $\boldsymbol{K}(\boldsymbol{K}')$ can fold and couple into the same $\boldsymbol{\Gamma}$ in tailored $\sqrt{3}N \times \sqrt{3}N$ or $3N \times 3N$ graphene superlattices by Bragg scattering from periodic adsorption [38]. Thus, a natural question arises: Through folding and coupling of two inequivalent valley phonons, can we get nondegenerate chiral phonons at the Brillouin-zone center? If yes, then one can easily detect the nondegenerate chiral phonons by Raman scattering. Here, we introduce $\sqrt{3} \times \sqrt{3}$ honeycomb superlattices by the periodic atomic mass doping, which may act as an option

*phyzlf@njnu.edu.cn

for electronics and phononics, especially for chirality phonon application.

In this paper, we study chiral phonons and its Berry phase effect in 2D $\sqrt{3}\times\sqrt{3}$ honeycomb superlattices. While in the honeycomb AB lattices all the phonons are nonchiral around the $\mathbf{\Gamma}$ point except the degenerate phonons exactly at $\mathbf{\Gamma}$ which can be chiral by superposition, in $\sqrt{3}\times\sqrt{3}$ superlattices, around the Brillouin-zone center we do observe right- or left-circularly polarized phonons with distinct energies. We also find that the chiral phonons have nonzero Berry curvature, which can induce transverse phonon transport under a strain gradient; thus, phonon Hall effect appears. In addition, we uncover a useful valley manipulation mechanism at $\mathbf{\Gamma}$ point by adjusting the doping sublattice's mass such that circularly polarized phonons can be engineered in specific branches. Finally, it is found that chiral phonons remain in the Brillouin-zone center if $\sqrt{3}\times\sqrt{3}$ honeycomb superlattices are deformed.

II. METHOD

In this section, we introduce the method for phonon polarization. To calculate the eigenmodes of phonons and get the Bloch-like eigenvectors, the periodic solution of lattice dynamics is set as

$$u_{l,\alpha}=m_{\alpha}^{-\frac{1}{2}}\varepsilon_{\alpha}(\boldsymbol{k})e^{i\boldsymbol{r}_{l,\alpha}\cdot\boldsymbol{k}},\quad \boldsymbol{r}_{l,\alpha}=\boldsymbol{R}_{l}+\boldsymbol{d}_{\alpha}, \tag{1}$$

where $\boldsymbol{R}_l$ and $\boldsymbol{d}_\alpha$ represent the equilibrium position of the lth unit cell and the αth atom in each unit cell, respectively. Thus, we have the dynamical matrix

$$D_{\alpha\alpha'}(\boldsymbol{k})=\sum_{\boldsymbol{R}_{l'}-\boldsymbol{R}_{l}}\frac{K_{l\alpha,l'\alpha'}}{\sqrt{m_{\alpha}m_{\alpha'}}}e^{i(\boldsymbol{R}_{l'}-\boldsymbol{R}_{l}+\boldsymbol{d}_{\alpha'}-\boldsymbol{d}_{\alpha})\cdot\boldsymbol{k}}. \tag{2}$$

In our mass-spring model, for the spring constant matrix K, only the neares-neighbor interactions are considered. The equation of motion can be written as

$$\omega_{\boldsymbol{k},\sigma}^{2}\varepsilon_{\alpha}(\boldsymbol{k},\sigma)=D_{\alpha\alpha'}(\boldsymbol{k})\varepsilon_{\alpha'}(\boldsymbol{k},\sigma); \tag{3}$$

here σ denotes different branch.

Since we consider phonon polarization along z direction (i.e., out of-plane direction) in which only 2D motion in $x-y$ plane has contribution, the phonon eigenvectors can be written as

$$\varepsilon=(x_1\ y_1\cdots x_n\ y_n)^T,\quad n=6, \tag{4}$$

which can be obtained from Eq. (3). In such a right-(left-) circular polarization basis:

$$\begin{aligned}
|R_1\rangle &\equiv \frac{1}{\sqrt{2}}(1\ i\ 0\cdots\ 0)^T,\\
|L_1\rangle &\equiv \frac{1}{\sqrt{2}}(1\ -i\ 0\cdots\ 0)^T,\\
&\vdots\\
|R_n\rangle &\equiv \frac{1}{\sqrt{2}}(0\cdots\ 0\ 1\ i)^T,\\
|L_n\rangle &\equiv \frac{1}{\sqrt{2}}(0\cdots\ 0\ 1\ -i)^T.
\end{aligned} \tag{5}$$

We can represent the phonon mode as

$$\varepsilon=\sum_{\alpha=1}^{n}\left(\varepsilon_{R_n}|R_n\rangle+\varepsilon_{L_n}|L_n\rangle\right), \tag{6}$$

where

$$\varepsilon_{R_n}=\langle R_n|\varepsilon\rangle,\quad \varepsilon_{L_n}=\langle L_n|\varepsilon\rangle. \tag{7}$$

The phonon polarization along the z direction can be defined as $S_{\rm ph}^{z}$. Under the operator for phonon polarization, we have

$$S_{\rm ph}^{z}=\sum_{\alpha=1}^{n}\left(|\varepsilon_{R_\alpha}|^2-|\varepsilon_{L_\alpha}|^2\right)\hbar. \tag{8}$$

Here, in the phonon polarization $S_{\rm ph}^{z}$ of a unit cell, each sublattice has a contribution of $S_{\alpha}^{z}=|\varepsilon_{R_\alpha}|^2-|\varepsilon_{L_\alpha}|^2$.

If a phonon has chirality, we can use phonon polarization $S_{\rm ph}^{z}$ to represent it. $S_{\rm ph}^{z}>0$, the phonon is right-handed; $S_{\rm ph}^{z}<0$, the phonon is left-handed.

From Eq. (3), the phonon wave function satisfies $D_{\alpha\alpha'}(\boldsymbol{k})\varepsilon_{\alpha'}(\boldsymbol{k},\sigma)=\omega_{\boldsymbol{k},\sigma}^{2}\varepsilon_{\alpha}(\boldsymbol{k},\sigma)$, in analogy to electron Berry curvature calculated from $H\psi_n=E_n\psi_n$, the phonon Berry curvature can be defined as [7,39]

$$\Omega_{k_xk_y}^{\sigma}=i\sum_{\sigma'\neq\sigma}\frac{\varepsilon_{\sigma}^{\dagger}\frac{\partial D}{\partial k_x}\varepsilon_{\sigma'}\varepsilon_{\sigma'}^{\dagger}\frac{\partial D}{\partial k_y}\varepsilon_{\sigma}-(k_x\leftrightarrow k_y)}{\left(\omega_{\sigma}^{2}-\omega_{\sigma'}^{2}\right)^2}. \tag{9}$$

III. RESULTS

A. Chiral phonons with fixed mass doping m_c

As shown in Fig. 1(a), our $\sqrt{3}\times\sqrt{3}$ superlattices are tailored on a honeycomb AB lattice by the periodic atomic mass doping of sublattice m_c. We can classify the six atoms in each primitive cell into three different categories by atomic mass: three atoms with m_a, two atoms with m_b, and one doping atom with m_c. If $m_c=m_b$, that is, we take the honeycomb AB superlattice with $\sqrt{3}\times\sqrt{3}$ periodicity, although the real unit cell is 1×1 (see Appendix A), all the valley chiral phonons are folded to Γ. However, such $\sqrt{3}\times\sqrt{3}$ superlattice is a hypothetical one, periodic doping is a feasible way to realize a $\sqrt{3}\times\sqrt{3}$ superlattice. For the isotopic doping, we can ignore the change in atomic bonding, thus first we only change the mass of the doping atoms without considering the changes of the interaction between them, thus our model can still maintain the basic orthohexagonal structure. For the spring constant matrix along the longitudinal direction, we take it as $\left(\begin{smallmatrix}K_L & 0\\ 0 & K_T\end{smallmatrix}\right)$, where $K_L=1$ and $K_T=0.25$, all other spring constant matrices can be obtained by rotation operators [20].

By obtaining the dynamic matrix of $\sqrt{3}\times\sqrt{3}$ honeycomb superlattices model, we can get the phonon dispersion relation. Since our model has six atoms in each unit cell and 2D motion is considered, there are twelve phonon branches, see Fig. 1(b). Here, we only focus on branches 5, 6, 7, and 8, which come from folding and splitting of branches 2 and 3 in honeycomb AB lattices [7]. The flat branches, nondiffusion localized vibration modes 6 and 7 are observed, which can be understood by the much bigger mass doping m_c. At $\mathbf{\Gamma}$ point, the lower and upper two branches are double degenerate. In Fig. 1(c), we get the nonzero phonon polarization of the four branches by inserting the eigenvectors into Eq. (8).

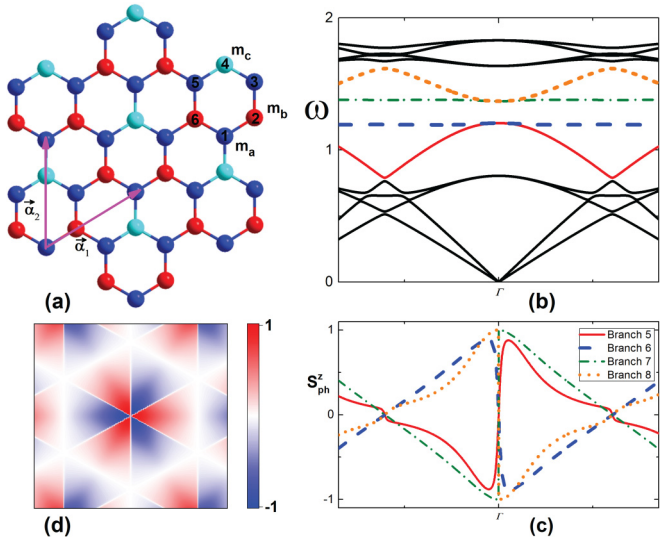

FIG. 1. (a) Schematic representation of the orthohexagonal $\sqrt{3}\times\sqrt{3}$ superlattices. The blue balls, red balls, and cyan balls represent sublattices 1, 3, and 5 with m_a, sublattices 2 and 6 with m_b, and sublattice 4 with m_c, respectively. The magenta lines represent lattice primitive cells basic vectors $\boldsymbol{\alpha}_1$ and $\boldsymbol{\alpha}_2$. (b), (c) Phonon dispersion and phonon polarization along the k_x-directions. The red solid, blue dash, olive dash dot, and orange short dash lines correspond to branches 5, 6, 7, and 8, respectively. (d) Contour plot denotes value of phonon polarization from -1 to $+1$ for branch 7. Here, $m_a = 1$, $m_b = 1.2$, and $m_c = 1.5$; the spring constants are $K_L = 1$ and $K_T = 0.25$.

Apparently, each branch's phonon polarization is an odd function of the wave vector in the k_x direction. Near $\boldsymbol{\Gamma}$, all four branches reach a maximum, and the trend of phonon polarization shows a type of jumping which has nonzero value. Especially for branches 7 and 8, the abrupt change of phonon polarization equals $\pm 1\hbar$. The phonon polarization for branch 7 in the Brillouin zone, which is invariant under a threefold rotation, is also shown in Fig. 1(d). As we see, the phonon polarization is zero in the valley $\boldsymbol{K}$ ($\boldsymbol{K}'$) regions, while they are concentrated in the Brillouin-zone center $\boldsymbol{\Gamma}$. Deserved to be mentioned, in honeycomb AB lattices, phonons have nearly no polarization in the Brillouin-zone center, when the phonon polarization reaches a maximum at the Brillouin-zone corners. Here, due to the folding of two inequivalent valleys, we do observe chiral phonons in the Brillouin-zone center of $\sqrt{3}\times\sqrt{3}$ honeycomb superlattices.

As shown in Fig. 1(c), near the $\boldsymbol{\Gamma}$ point, the phonon polarization of $\pm 1\hbar$ will appear in the upper two branches 7 and 8. From the analysis of eigenvectors shown in Fig. 2, the upper two branches 7 and 8 come from the folding of branch 3 in the original honeycomb AB lattice, and at $\boldsymbol{\Gamma}$ point the atoms inherit the circular vibrations from those at $\boldsymbol{K}$ of original honeycomb AB lattice; that is, in a unit cell atoms 1, 3, and 5 make circular vibrations while the other atoms stay still. In this model, we keep the atomic bonding independent on atom mass, thus the atoms 1, 3, and 5 feel no change after doping and keep the original vibration, i.e., the phonon polarization of branches 7, 8 keep $\pm 1\hbar$ which comes from the simple folding of phonon modes at $\boldsymbol{K}$ of original honeycomb AB lattice.

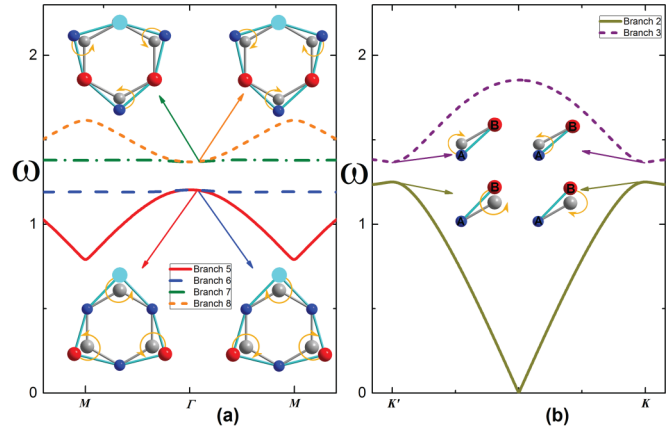

FIG. 2. At a fixed point ($k_x = \frac{1}{10a}$, $k_y = 0$) near the zone center $\boldsymbol{\Gamma}$. (a) Phonon vibration modes of branches 5, 6, 7 and 8 in $\sqrt{3}\times\sqrt{3}$ honeycomb superlattices. (b) Phonon vibration modes of branches 2 and 3 in honeycomb AB lattices. The gray balls represent original location of all sublattices in a unit cell, the arrow denotes rotation direction. Here, $m_a = 1$, $m_b = 1.2$ and $m_c = 1.5$; the spring constants are $K_L = 1$ and $K_T = 0.25$.

For the lower two branches 5 and 6, very close to $\boldsymbol{\Gamma}$, the phonon polarization comes to zero which is different from those of branches 7 and 8. Similar to the analysis above, as shown in Fig. 2, the lower two branches 5 and 6 come from the folding of branch 2 in the original honeycomb AB lattice, in a unit cell at $\boldsymbol{\Gamma}$ point atoms 2, 4, and 6 make circular vibrations while the other atoms stay still, which is similar to the modes at $\boldsymbol{K}$ in original honeycomb AB lattice where only atom 2 vibrates. However, the mass changing of atom 4 which introduces valley interaction when the two degenerated valleys fold to the same point of $\boldsymbol{\Gamma}$, such interaction kills the phonon polarization. Away from the Brillouin center, the phonon polarization remains since the valley interaction plays a less important role.

Here we discuss the topological properties of chiral phonons in the Brillouin zone center of $\sqrt{3}\times\sqrt{3}$ honeycomb superlattice structures. The phonon Berry curvature of

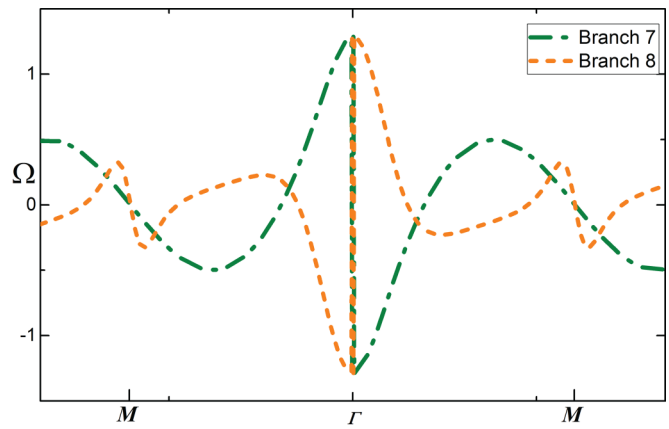

FIG. 3. The phonon Berry curvature of branches 7 and 8 along the k_x-directions. Here, $m_a = 1$, $m_b = 1.2$ and $m_c = 1.5$; the spring constants are $K_L = 1$ and $K_T = 0.25$.

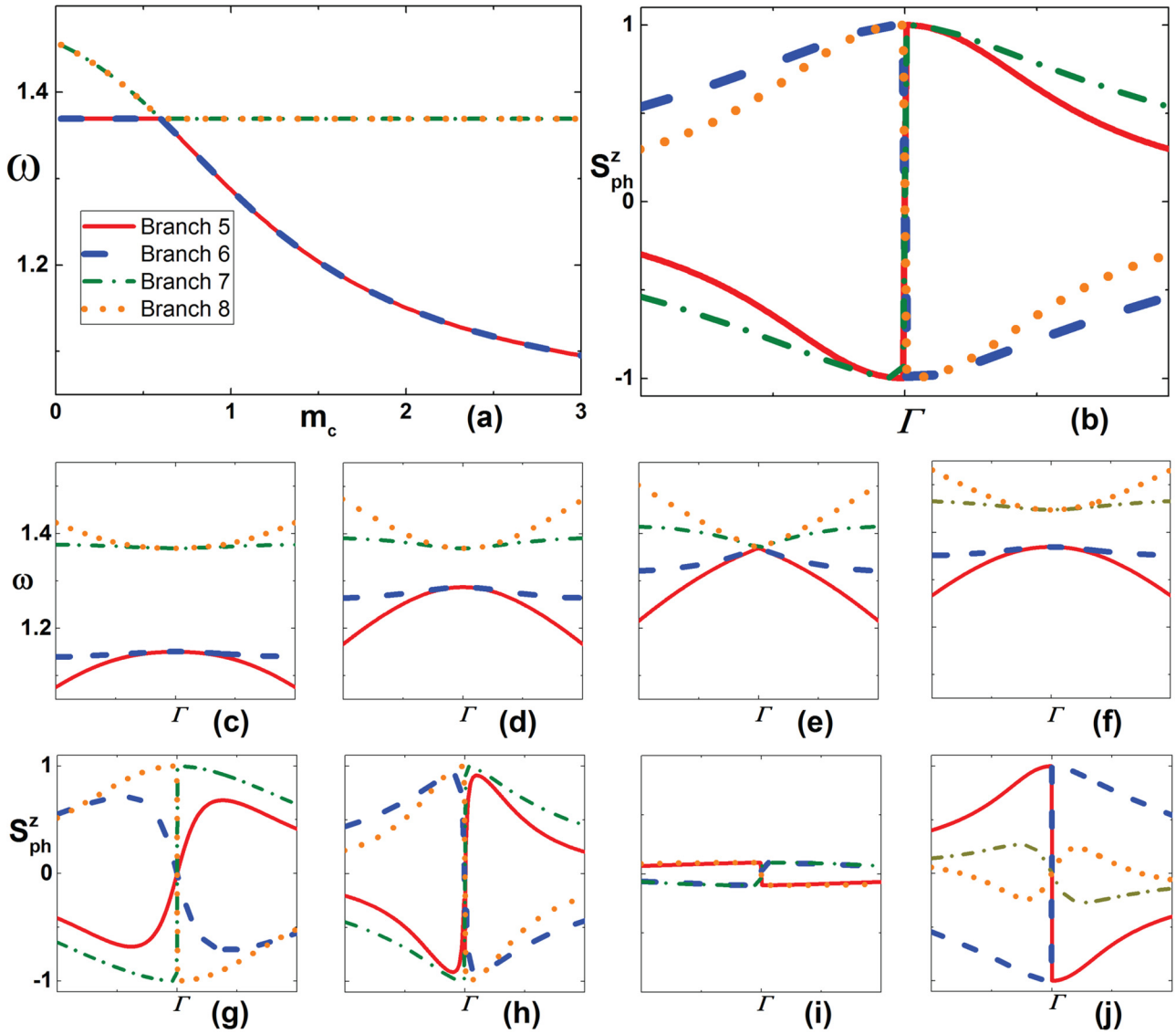

FIG. 4. (a) At the **Γ** point, phonon dispersion of branches 5, 6, 7, and 8 versus m_c. (b) The phonon polarization of the four branches when $m_c = 1.2$. (c)–(f) The phonon dispersion relation of the four branches at $m_c = 2.0$, 1.0, 0.6, and 0.1, respectively. (g)–(j) The phonon polarization of the four branches at $m_c = 2.0$, 1.0, 0.6, and 0.1, respectively. Here, $m_a = 1$ and $m_b = 1.2$; the spring constants are $K_L = 1$ and $K_T = 0.25$.

branches 7 and 8 along the k_x directions are reported in Fig. 3. As we see, the nonzero Berry curvature is the odd function of the wave vector, which can be understood by the the preservation of time-reversal symmetry in our model. With the integral of the Berry curvature, the Chern numbers of the two branches are zero. An abrupt change point appears at the **Γ** which the Berry curvature is maximum, thus the circularly polarized chiral phonons have relatively large nonzero Berry curvature here. Such chiral phonons exist near the Brillouin center, and thus can be vastly excited by Raman scattering. If we apply a strain gradient or even a temperature gradient, the nonzero Berry curvature can give chiral phonons an anomalous velocity, thus one can observe a phonon Hall effect contributed from phonons near the Brillouin-zone center **Γ** although the system is topologically trivial.

B. A valley manipulation mechanism by adjusting m_c

As mentioned before, we obtain chiral phonons in the Brillouin-zone center by introducing periodic mass doping m_c. At **Γ** point, we find that the phonon frequency is indeed related to the m_c and the lower and upper two branches are always double degenerate, see Fig. 4(a). When $m_c = 1.2$, our model turns to an original honeycomb AB lattice, and the only difference is that we choose a triple-size unit which has six atoms, thus all the chiral phonons at ***K*** are simply folded to **Γ**, near **Γ**, the phonons have maximum polarizations of ± 1, see Fig. 4(b). As discussed in the above session, branches 7 and 8 correspond to vibrations of light atoms 1, 3, and 5 while branches 5 and 6 denote the vibrations of heavy atoms 2, 4, and 6, thus we can call them light phonons (branches 7 and 8) and heavy phonons (branches 5 and 6). If

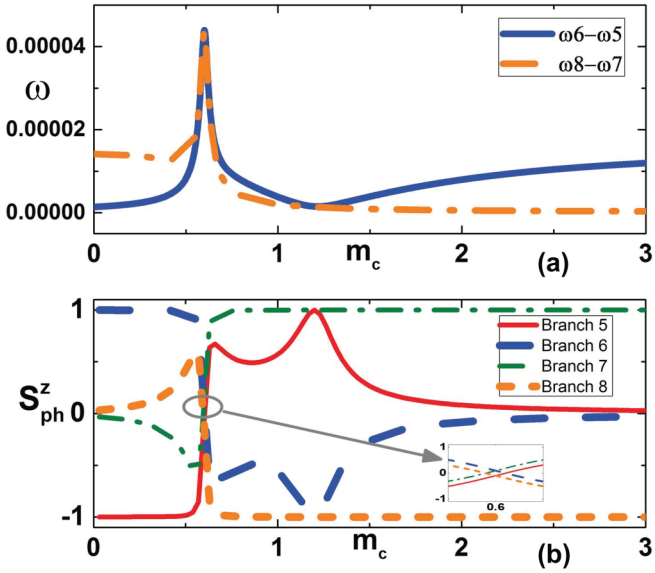

FIG. 5. (a) The phonon frequency difference between branches 5 and 6, branches 7 and 8 changes versus m_c at a fixed point ($k_x = \frac{1}{100a}$, $k_y = 0$) which is near zone center $\mathbf{\Gamma}$. (b) The phonon polarization of the four branches changes versus m_c at a fixed point ($k_x = \frac{1}{100a}$, $k_y = 0$). The inset shows a part of the phonon polarization in the k_x direction (from $k_x = -\frac{1}{2a}$ to $k_x = \frac{1}{2a}$). Here, $m_a = 1$ and $m_b = 1.2$; the spring constants are $K_L = 1$ and $K_T = 0.25$.

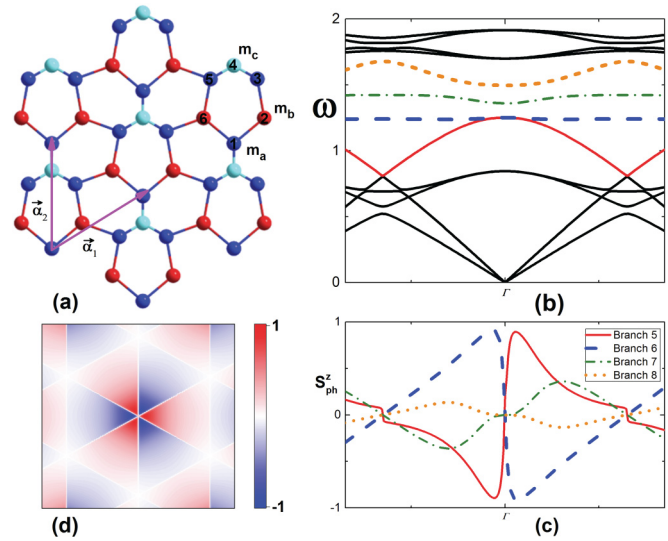

FIG. 6. (a) Schematic representation of the deformed $\sqrt{3} \times \sqrt{3}$ superlattices. (b), (c) Phonon dispersion and phonon polarization along the k_x directions. (d) Contour plot of the phonon polarization for branch 5. Here, $m_a = 1$, $m_b = 1.2$ and $m_c = 1.5$; the spring constants are $K_L = 1$ and $K_T = 0.25$.

we increase the doping mass $m_c > 1.2$, as shown in Fig. 4(c), the light phonons and heavy phonons keep double degenerate, respectively, but the gap between them increases. The phonon polarization of branches 7 and 8 keep ± 1 while the polarization of branches 5 and 6 goes to zero near Γ due to the valley interaction as discussed above, as shown in Fig. 4(g). When we decrease the doping mass but $m_c > 0.6$, as shown in Fig. 4(d), the four branches keep double degenerate but the gap between them decreases since the heavy phonon becomes lighter, i.e., the frequency increases due to the mass decrease. Before gap closing, the heavy phonons are separated from the light ones, and the phonon polarization shown in Fig. 4(h) has a behavior similar to that in Fig. 4(g). If the mass of the doping atom decreases to 0.6, the gap between the light and heavy phonons closes, as shown in Fig. 4(i), the four branches are degenerate at Γ, which introduces interaction to light phonons, and all the phonon polarization goes to zero near Γ. When m_c is less than 0.6, then the bands invert, the original heavy phonons become light with a higher frequency (branches 5 and 6), and the original light phonons become heavy with a lower frequency (branches 5 and 6) as shown in Fig. 4(f), thus the phonon polarization of doubly degenerate branches 5 and 6 equals ± 1, while the other two degenerate branches have a relatively small polarization.

For the two double degenerate phonons, one is longitudinal optical (LO) mode, the other is transverse optical (TO) mode, they are degenerate at the Γ point, and split at wave vectors away from Γ. The LO/TO splitting is affected by the doping [40]. Here we discuss the TO/LO splitting effect on the phonon polarization near to Γ, as shown in Fig. 5. Due to mass doping, m_c has no change on atomic bonding; before branches inverting at $m_c = 0.6$, the light phonons (branches 7 and 8) keep circularly polarized (with a maximum polarization ± 1) and after the inverting ($m_c < 0.6$) the lower two phonons (branches 5 and 6) have maximum polarization ± 1, and the LO/TO splitting is almost zero, as shown in Fig. 5(a) (see the solid-dot line at $m_c > 0.6$ and the solid line at $m_c < 0.6$). If $m_c < 0.6$, branches 7 and 8 have a small polarization due to the large LO/TO splitting. For branches 5 and 6, they have maximum polarization at $m_c = 1.2$ where the LO/TO splitting is almost zero; if $m_c \neq 1.2$, the phonon polarization decreases when the LO/TO splitting increases. However, near $m_c = 0.6$, due to the branch inversion and strong interaction, the monotonous relation between LO/TO splitting and phonon polarization does not apply. Therefore, for the chiral phonons' folded valley to Brillouin center, except the Γ point, mostly we can find a large phonon polarization if the LO/TO splitting is small.

C. Chiral phonons in a deformed $\sqrt{3} \times \sqrt{3}$ superlattice

If the doping atom is not isotopic, then the force constants will change, thus the $\sqrt{3} \times \sqrt{3}$ honeycomb superlattice will be deformed. There are two kinds of springs, one is the spring between m_b and m_a (m_b-centered interaction), another is the one between m_c and m_a (m_c-centered interaction). Since m_a is taken to be 1, to mimic the difference between the spring constants, we take the spring constant matrices between m_a and m_α as $K_{a\alpha} = \begin{pmatrix} \sqrt[3]{m_\alpha} K_L & 0 \\ 0 & \sqrt[3]{m_\alpha} K_T \end{pmatrix}$, where $\alpha = b, c$, $K_L = 1$, $K_T = 0.25$. The deformed structure is confirmed by the first-principles calculation (see Appendix B), the ortho-hexagonal honeycomb primitive cell occur deformation to ensure the structure optimization here, see Fig. 6(a). Similarly, the phonon dispersion relation and phonon polarization of branches 5, 6, 7, and 8 are illustrated in Figs. 6(b) and 6(c). Branches 5 and 6 correspond to heavy atoms 2, 4, and 6, which are the same with those in nondeformed lattice

discussed above, the phonon polarization of the branches 5, 6 can't get ± 1 because the mass doping of m_c produced a weak intervalley interaction, which means the phonon is elliptically polarized here. The contour plot of the phonon polarization for branch 5 also presented a threefold rotation symmetry, and concentrated in the $\mathbf{\Gamma}$ regions. However, due to the atomic bonding change, which introduces a strong intervalley interaction when the valley phonons are folded to Γ, and such strong interaction makes branches 7 and 8 be nondegenerate at $\mathbf{\Gamma}$ point. Therefore, branch 7 and 8 phonons have a rather small value of polarization due to the abrupt LO/TO splitting. Although some chiral phonons are killed by the valley interaction in the deformed $\sqrt{3} \times \sqrt{3}$ honeycomb superlattice, we do also observe chiral phonons around the Brillouin-zone center.

IV. CONCLUSION

We study phonon chirality and its topological properties in an orthohexagonal $\sqrt{3} \times \sqrt{3}$ honeycomb superlattice. For the middle four branches, which come from folding and splitting of branches 2 and 3 in honeycomb AB lattices, we do observe right or left chiral phonons with distinct energies around the Brillouin-zone center $\mathbf{\Gamma}$. By discussing the contribution of each sublattice in a unit cell to the total phonon polarization, we conclude that the intervalley interaction at Γ, which folded two inequivalent valleys, is vital to study circularly polarized phonon modes. For the chiral phonons, we find that they have nonzero phonon Berry curvature, thus the phonon Hall effect can be proposed with a strain gradient. Furthermore, we uncover a useful valley manipulation mechanism at $\mathbf{\Gamma}$ point by adjusting the doping sublattice's mass. Thus, circularly polarized phonons can be engineered in specific branches. We also find that the larger LO/TO splitting makes the phonon polarization be smaller. Finally, even in a deformed $\sqrt{3} \times \sqrt{3}$ honeycomb superlattice, we also observe chiral phonons.

ACKNOWLEDGMENT

This work is supported by NSFC (Grant No. 11574154).

APPENDIX

1. Chiral phonons in honeycomb AB superlattices

In our calculation of chiral phonons, we also consider a special honeycomb AB superlattice with $\sqrt{3} \times \sqrt{3}$ periodicity, although the real unit cell is 1×1, as shown in Fig. 7(a). Here, $m_c = 1.2$ and each sublattice keeps its threefold rotation symmetry. The phonon dispersion relation and phonon polarization of branches 5, 6, 7, and 8 are illustrated in Figs. 7(b) and 7(c). Similarly, the lower and upper two branches are double degenerated at $\mathbf{\Gamma}$ point and the middle four branches' phonon polarization is an odd function of the wave vector in the k_x direction. In the process of the two inequivalent valleys folding to the same $\mathbf{\Gamma}$, the lower and upper two branches cannot only keep consistent with the honeycomb AB lattices' vibration modes of branches 2 and 3, but also inherit the motion properties of the circular polarization. Thus, all four branches have the polarization of ± 1 at $\mathbf{\Gamma}$ point, which is different from the $\sqrt{3} \times \sqrt{3}$ honeycomb superlattices with

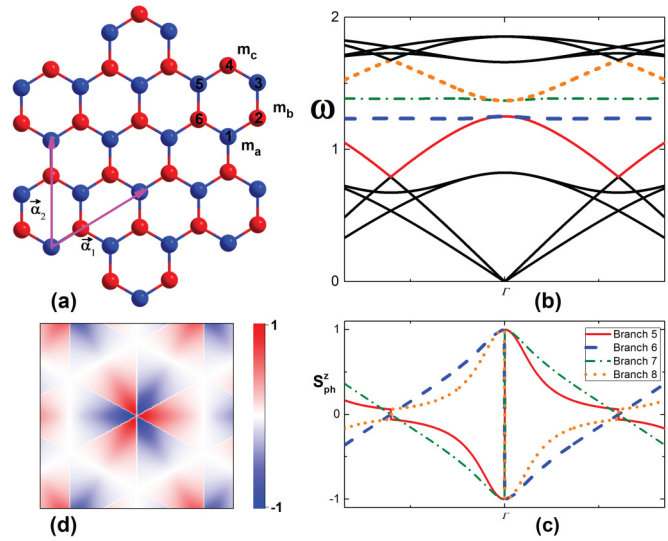

FIG. 7. (a) Schematic representation of the honeycomb AB superlattices. The blue balls and red balls represent sublattices 1, 3, and 5 with m_a, sublattices 2, 4, and 6 with m_b, respectively. The magenta lines represent lattice primitive cells basic vectors $\boldsymbol{\alpha}_1$ and $\boldsymbol{\alpha}_2$. (b), (c) Phonon dispersion and phonon polarization along the k_x directions. The red solid, blue dash, olive dash dot, and orange short dash lines correspond to branches 5, 6, 7, and 8, respectively. (d) Contour plot of the phonon polarization for branch 7. Here, $m_a = 1$ and $m_b = 1.2$; the spring constants are $K_L = 1$ and $K_T = 0.25$.

mass doping of m_c, where the intervalley interaction increases the LO/TO splitting and decreases the phonon polarization near the $\mathbf{\Gamma}$ point. The contour plot of the phonon polarization for branch 7 have also presented a threefold rotation symmetry, and concentrated in the $\mathbf{\Gamma}$ regions, see Fig. 7(d). As a conclusion, due to the folding and coupling of two inequivalent valleys, we do observe chiral circular phonons in the Brillouin-zone center of honeycomb AB superlattices.

2. The first-principles calculation

As shown in Fig. 8, we dope one silicon atom on the hexagonal boron nitride structure. The structure is calculated

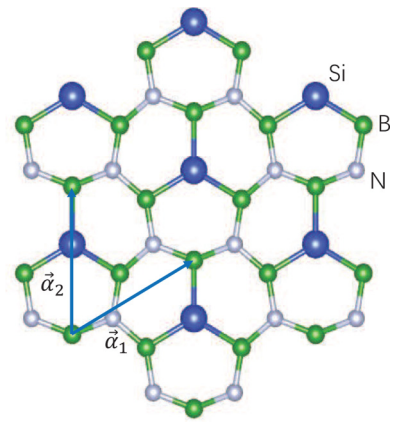

FIG. 8. The structure of one unit cell of hexagonal boron nitride structure with doping of one silicon atom.

by the Quantum Espresso code [41], where the local density approximation is used for the exchange and correlation energy functional. The normcons pseudopotentials are used, and the kinetic energy cutoff for wave functions is 60 Ry. Within the framework of density functional perturbation theory, the dynamical matrices are calculated using a $9 \times 9 \times 1$ q-point mesh. For this structure, the lattice parameter is 4.87.

[1] A. Einstein and W. J. de Haas, Koninklijke Nederlandsche Akademie van Wetenschappen Proceedings **18**, 696 (1915).
[2] V. Ya Frenkel, Sov. Phys. Usp. **22**, 580 (1979).
[3] C. J. Davisson and J. W. Beams, Rev. Mod. Phys. **25**, 246 (1953).
[4] C. Kittel, Phys. Rev. **76**, 743 (1949).
[5] R. A. Reck and D. L. Fry, Phys. Rev. **184**, 492 (1969).
[6] L. Zhang and Q. Niu, Phys. Rev. Lett. **112**, 085503 (2014).
[7] L. Zhang and Q. Niu, Phys. Rev. Lett. **115**, 115502 (2015).
[8] D. Xiao, W. Yao, and Q. Niu, Phys. Rev. Lett. **99**, 236809 (2007).
[9] W. Yao, D. Xiao, and Q. Niu, Phys. Rev. B **77**, 235406 (2008).
[10] D. Xiao, G.-B. Liu, W. Feng, X. Xu, and W. Yao, Phys. Rev. Lett. **108**, 196802 (2012).
[11] T. Cao, G. Wang, W. Han, H. Ye, C. Zhu, J. Shi, Q. Niu, P. Tan, E. Wang, B. Liu, and J. Feng, Nat. Commun. **3**, 887 (2012).
[12] Q. H. Wang, K. Kalantar-Zadeh, A. Kis, J. N. Coleman, and M. S. Strano, Nat. Nanotechnol. **7**, 699 (2012).
[13] K. F. Mak, K. He, J. Shan, and T. F. Heinz, Nat. Nanotechnol. **7**, 494-498 (2012).
[14] H. Zeng, J. Dai, W. Yao, D. Xiao, and X. Cui, Nat. Nanotechnol. **7**, 490 (2012).
[15] S. Wu, S. Buckley, A. M. Jones, J. S. Ross, N. J. Ghimire, J. Yan, D. G. Mandrus, W. Yao, F. Hatami, J. Vuckovic, A. Majumdar, and X. Xu, Nat. Phys. **9**, 149 (2013).
[16] A. M. Jones, H. Yu, N. J. Ghimire, S. Wu, G. Aivazian, J. S. Ross, B. Zhao, J. Yan, D. G. Mandrus, D. Xiao, W. Yao, and X. Xu, Nat. Nanotechnol. **8**, 634 (2013).
[17] X. Xu, W. Yao, D. Xiao, and T. F. Heinz, Nat. Phys. **10**, 343 (2014).
[18] D. Liu and J. Shi, Phys. Rev. Lett. **119**, 075301 (2017).
[19] Y. Liu, C.-S. Lian, Y. Li, and Y. Xu, and W. Duan, Phys. Rev. Lett. **119**, 255901 (2017).
[20] X. Xu, W. Zhang, J. Wang, and L. Zhang, J. Phys.: Condens. Matter **30**, 225401 (2018).
[21] M. Gao, W. Zhang, and L. Zhang, Nano Lett. **18**, 4424 (2018).
[22] H. Zhu, J. Yi, M. Li, J. Xiao, L. Zhang, C. Yang, R. A. Kaindl, L. Li, Y. Wang, and X. Zhang, Science **359**, 579 (2018).
[23] J. Wang, H. Chen, G. Xiong, X. Xu, and L. Zhang, New J. Phys. **20**, 073006 (2018).
[24] Y. Xing, X. Xu, and L. Zhang, Acta Phys. Sinica **66**, 226601 (2017).
[25] H. Yu, X. Xu, Q. Niu, and L. Zhang, Acta Phys. Sinica **67**, 076302 (2018).
[26] G. Jotzu, M. Messer, R. Desbuquois, M. Lebrat, T. Uehlinger, D. Greif, and T. Esslinger, Nature **515**, 237 (2014).
[27] M. Rini, R. Tobey, N. Dean, Y. Tomioka, Y. Tokura, R. W. Schoenlein, and A. Cavalleri, Nature **449**, 72 (2007).
[28] M. Först, R. Mankowsky, and A. Cavalleri, Acc. Chem. Res. **48**, 380 (2015).
[29] J. R. Schaibley, H. Yu, G. Clark, P. Rivera, J. S. Ross, K. L. Seyler, W. Yao, and X. D. Xu, Nat. Rev. Mat. **1**, 16055 (2016).
[30] K. F. Mak, K. L. McGill, J. Park, and P. L. McEuen, Science **344**, 1489 (2014).
[31] Y. J. Zhang, T. Oka, R. Suzuki, J. T. Ye, and Y. Iwasa, Science **344**, 725 (2014).
[32] H. Katsuki, J. C. Delagnes, K. Hosaka, K. Ishioka, H. Chiba, E. S. Zijlstra, M. E. Garcia, H. Takahashi, K. Watanabe, M. Kitajima, Y. Matsumoto, K. G. Nakamura, and K. Ohmori, Nat. Commun. **4**, 3801 (2013).
[33] B. R. Carvalho, Y. Wang, S. Mignuzzi, D. Roy, M. Terrones, C. Fantini, V. H. Crespi, L. M. Malard, and M. A. Pimenta, Nat. Commun. **8**, 14670 (2013).
[34] K. C. Lee, M. R. Sprague, B. J. Sussman, J. Nunn, N. K. Langford, X.-M. Jin, T. Champion, P. Michelberger, K. F. Reim, and D. England, Science **334**, 1253 (2011).
[35] A. Srivastava, M. Sidler, A. V. Allain, D. S. Lembke, and A. Kis, Nat. Nano. **10**, 491 (2015).
[36] T. Low, A. Chaves, J. D. Caldwell, A. Kumar, N. X. Fang, P. Avouris, T. F. Heinz, F. Guinea, L. Martin-Moreno, and F. Koppens, Nat. Mater. **16**, 182 (2016).
[37] S.-Y. Chen, C. Zheng, M. S. Fuhrer, and J. Yan, Nano Lett. **15**, 2526 (2015).
[38] Y. Ren, X. Deng, Z. Qiao, C. Li, J. Jung, C. Zeng, and Z. Zhang, and Q. Niu, Phys. Rev. B **91**, 245415 (2015).
[39] L. Zhang, J. Ren, J.-S. Wang, and B. Li, Phys. Rev. Lett. **105**, 225901 (2010).
[40] T. Sohier, M. Gibertini, M. Calandra, F. Mauri, and N. Marzari, Nano Lett. **17**, 3758 (2017).
[41] P. Giannozzi, S. Baroni, N. Bonini, M. Calandra, R. Car, C. Cavazzoni, D. Ceresoli, G. L. Chiarotti, M. Cococcioni, I. Dabo *et al.*, J. Phys.: Condens. Matter **21**, 395502 (2009).